

Computational Fluid Dynamics of a Radial Compressor Operating With Supercritical CO₂

Rene Pecnik¹

e-mail: r.pecnik@tudelft.nl

Enrico Rinaldi

Piero Colonna

Process and Energy Department,
Delft University of Technology,
Leeghwaterstraat 44, 2628 CA Delft,
The Netherlands

The merit of using supercritical CO₂(scCO₂) as the working fluid of a closed Brayton cycle gas turbine is now widely recognized, and the development of this technology is now actively pursued. scCO₂ gas turbine power plants are an attractive option for solar, geothermal, and nuclear energy conversion. Among the challenges that must be overcome in order to successfully bring the technology to the market is that the efficiency of the compressor and turbine operating with the supercritical fluid should be increased as much as possible. High efficiency can be reached by means of sophisticated aerodynamic design, which, compared to other overall efficiency improvements, like cycle maximum pressure and temperature increase, or increase of recuperator effectiveness, does not require an increase in equipment cost, but only an additional effort in research and development. This paper reports a three-dimensional computational fluid dynamics (CFD) study of a high-speed centrifugal compressor operating with CO₂ in the thermodynamic region slightly above the vapor–liquid critical point. The investigated geometry is the compressor impeller tested in the Sandia scCO₂ compression loop facility. The fluid dynamic simulations are performed with a fully implicit parallel Reynolds-averaged Navier–Stokes code based on a finite volume formulation on arbitrary polyhedral mesh elements. In order to account for the strongly nonlinear variation of the thermophysical properties of supercritical CO₂, the CFD code is coupled with an extensive library for the computation of properties of fluids and mixtures. A specialized look-up table approach and a meshing technique suited for turbomachinery geometries are also among the novelties introduced in the developed methodology. A detailed evaluation of the CFD results highlights the challenges of numerical studies aimed at the simulation of technically relevant compressible flows occurring close to the liquid–vapor critical point. The data of the obtained flow field are used for a comparison with experiments performed at the Sandia scCO₂ compression-loop facility. [DOI: 10.1115/1.4007196]

Introduction

The concept of exploiting the small compression work occurring in a closed Brayton cycle operated with scCO₂ in order to obtain high conversion efficiency at moderate maximum cycle temperature was studied in the 1960s [1,2], and was successfully resumed more recently; see, e.g., Ref. [3]. These studies led to the realization of a small-scale proof-of-concept prototype documented, e.g., in Ref. [4]. Once operating pressures and temperatures are fixed by technological requirements on the materials of the primary heat exchanger and of the recuperator, the overall conversion efficiency strongly depends on the efficiency of turbomachinery. In this respect aerodynamic design is of paramount importance.

While there has been enormous progress in the design of turbomachinery operated on steam and air, fluids behaving like ideal gases, there have been only a few studies covering the unconventional flow behavior of fluids whose thermodynamic properties are in the range of the vapor–liquid critical point [5–7]. Often, the design of the turbomachinery components operating with supercritical fluids is based on one-dimensional models taking into account real gas effects by means of surrogate fluid models [4]. Fluid properties close to the critical point strongly deviate from the ideal gas law and, even more importantly, exhibit strong variations. Flows whose thermodynamic properties encompass the critical region are, therefore, highly unconventional and the gas dynamics of dense and supercritical fluids remain largely unex-

plored. The aerodynamic design and verification of turbomachinery operating in the close-to-critical region can greatly benefit from high-fidelity flow simulations. This study is part of a project aimed at developing and validating CFD codes that can be used as an aid in the design and performance verification of turbomachinery operated in the supercritical thermodynamic region.

The paper is structured as follows. First the real-gas Navier–Stokes solver is briefly presented, followed by the treatment of the calculation of the fluid's thermodynamic properties. A short description of the impeller geometry and the computational mesh is given afterwards. Next, the results of the simulation at a given nominal compressor operating condition are analyzed. Finally a range of operating conditions is investigated by keeping the rotational speed and the impeller inlet conditions constant, while the exit pressure is varied. The ideal head coefficient and the efficiency as a function of the flow coefficient are qualitatively compared to the experimental results. Concluding remarks summarize the results of the study and outline future work.

Real-Gas Navier–Stokes Solver

A parallel solver for the solution of the compressible Navier–Stokes equations on unstructured meshes based on a finite volume formulation and implicit time-integration on arbitrary polyhedral meshes has been used. The code solves the Favre-averaged Navier–Stokes equations and is entirely written in C++ and uses subdomain decomposition and the Message Passing Interface as the parallel infrastructure [8,9]. Two different turbulence models are implemented in the code, namely the one-equation eddy viscosity model of Spalart and Allmaras [10] and the two-equation $k-\omega$ shear-stress-transport (SST) turbulence model of Menter [11].

¹Corresponding author.

Contributed by International Gas Turbine Institute (IGTI) of ASME for publication in the JOURNAL OF ENGINEERING FOR GAS TURBINES AND POWER. Manuscript received June 19, 2012; final manuscript received July 5, 2012; published online October 11, 2012. Editor: Dilip R. Ballal.

The governing equations are written in the conservative form as

$$\frac{\partial}{\partial t} \int_{\Omega} \mathbf{U} d\Omega + \int_{\partial\Omega} [\mathbf{F}(\mathbf{U}) - \mathbf{F}_v(\mathbf{U})] dA = \int_{\Omega} \mathbf{S} d\Omega \quad (1)$$

where $\mathbf{U} = \mathbf{U}(\mathbf{x}, t)$ is the state variable, $\mathbf{F}(\mathbf{U})$ and $\mathbf{F}_v(\mathbf{U})$ are the convective and viscous fluxes, respectively, and Ω and $\partial\Omega$ are the physical domain of interest and its boundary.

In particular, we consider the fluxes for a rotating noninertial reference frame:

$$\mathbf{U} = \begin{bmatrix} \rho \\ \rho \mathbf{v} \\ \rho e^t \end{bmatrix}, \quad \mathbf{F}(\mathbf{U}) = \begin{bmatrix} \mathbf{n} \cdot \rho(\mathbf{v} - \mathbf{v}^m) \\ \rho \mathbf{v}[\mathbf{n} \cdot (\mathbf{v} - \mathbf{v}^m)] + P \mathbf{n} \\ (\rho e^t + P)[(\mathbf{v} - \mathbf{v}^m) \cdot \mathbf{n}] + P(\mathbf{v}^m \cdot \mathbf{n}) \end{bmatrix},$$

$$\mathbf{F}_v(\mathbf{U}) = \begin{bmatrix} 0 \\ \mathbf{n} \cdot \Pi \\ \mathbf{v} \cdot (\mathbf{n} \cdot \Pi) + \mathbf{n} \cdot (\lambda \nabla T) \end{bmatrix}, \quad \mathbf{S}(\mathbf{U}) = \begin{bmatrix} 0 \\ -\rho(\omega \times \mathbf{v}) \\ 0 \end{bmatrix} \quad (2)$$

with the density ρ , Cartesian velocity vector \mathbf{v} , velocity of the rotating noninertial reference frame $\mathbf{v}^m = \omega \times \mathbf{r}$, pressure P , total energy ρe^t , stress tensor Π , thermal conductivity λ , temperature T , and outward pointing unit vector normal to the surface \mathbf{n} .

The flow quantities are stored in the cell centers and the governing equations are integrated implicitly in conservative form:

$$\frac{\partial \mathbf{U}}{\partial t} = -\mathbf{R}(\mathbf{U}), \quad \text{with: } \mathbf{R}(\mathbf{U}) = \frac{1}{V} \sum_f [\mathbf{F}(\mathbf{U}) - \mathbf{F}_v(\mathbf{U})] A_f - \mathbf{S}(\mathbf{U}) \quad (3)$$

The large sparse system (the Jacobian matrices are obtained using first-order discretization) is solved with the generalized minimal residual method, preconditioned with the incomplete lower-upper (ILU) factorization, using the freely available linear solver package PETSc [12].

Higher-Order Gradient Reconstruction

Second-order accuracy is typically achieved in the finite volume context by computing the states at each side of a given cell face using second-order interpolation and then applying the same flux evaluation scheme to the reconstructed states. On an unstructured grid the reconstruction is formulated as

$$\phi_f^L = \phi_P + \psi_P \nabla \phi|_P \cdot \mathbf{r}_f \quad (4)$$

where $\nabla \phi|_P$ is a discrete approximation of the gradient at the cell center P , computed using a standard least-squares approximation, ψ_P is the slope-limiter function, and \mathbf{r}_f is the vector connecting the cell center and the center of the face f . Across a discontinuity and, in general, in regions where the solution changes rapidly, the slope-limiter function ψ_P reduces the discrete gradient such that the reconstructed value at the face center maintains monotonicity. Slope limiters are reviewed in Ref. [13] as well as issues that can arise in case of unstructured grids. We implemented the limiter procedure first proposed in Ref. [14], and later improved by Venkatakrishnan [15]. Further modifications were proposed by one of the authors and are summarized in Ref. [8].

Convective Fluxes

In the past three decades, many different approaches have been introduced to evaluate convective fluxes. In general, for compressible flow simulation approximate Riemann solvers are most com-

monly used. These solvers approximate the wavespeeds (eigenvalues of the Jacobian matrix) from an arithmetic or a square-root average of the left and right states of the Riemann problem [16]. This procedure leads to several errors, which are the underestimation of the expansion-wave velocity (expansion shock) and instabilities close to the stagnation point of supersonic flows (carbuncle phenomenon) [17,18]. Different solutions have been proposed in the literature and can be separated into two families: eigenvalue-limiting methods and hybrid approaches, given in Refs. [19,20]. The approximate Riemann solver used in the present context is the advection upstream splitting method (AUSM) scheme proposed by Ref. [21]. In this method the entropy condition is enforced (no entropy violating discontinuous waves, called rarefaction shocks), and the scheme preserves positivity without the need for additional corrections.

Furthermore, it is important to satisfy the equation of state at the cell faces for the evaluation of the convective fluxes. In the present context the primitive variables: density ρ , pressure p , and the velocity vector \mathbf{v} are extrapolated towards the face centers using Eq. (4). Additional quantities that are needed for the flux evaluation (speed of sound, pressure derivatives for the Jacobi matrices) are then computed using these reconstructed values in order to maintain thermodynamic consistency.

Viscous Fluxes

The viscous fluxes contain second derivatives of the velocity \mathbf{u} and the enthalpy h . Therefore, gradients at the cell face need to be calculated in an efficient and accurate way. Consider the scalar quantity ϕ whose gradient at the cell face is $\nabla \phi$. We approximate the normal gradient at the face as

$$\nabla \phi|_f \cdot \mathbf{n}_f = \frac{\phi_{nbr} - \phi_P}{|\mathbf{x}_{nbr} - \mathbf{x}_P|} \alpha_f + \frac{1}{2} (\nabla \phi|_P + \nabla \phi|_{nbr}) \cdot (\mathbf{n}_f - \alpha_f \mathbf{s}_f) \quad (5)$$

where the subscript f indicates the face with the adjacent control volumes P and its neighbor nbr [22]. The vector \mathbf{n} is the face normal and \mathbf{s} is the normalized vector connecting the cell centroid across the face f . The gradients $\nabla \phi$ at the cell centers are computed using the limited least-squares approximation (as described in the section Higher-Order Gradient Reconstruction above) and α is chosen to be the dot product $\alpha = \mathbf{s} \cdot \mathbf{n}$.

Thermodynamic Model and Table Look-Up

A rich thermodynamic library for the calculation of properties and their partial derivatives, with respect to density and internal energy (required by the implicit solution procedure for the Navier–Stokes equations) of pure fluids and mixtures, has been used [5,23]. The library provides a standard interface to sublibraries, either proprietary or provided by third parties (e.g., Ref. [24]). It is notable that a number of secondary thermodynamic properties, a combination of partial derivative of primary properties like P, T, ρ, h, s , are provided in addition to standard primary properties and are computed analytically for each available thermodynamic model.

In the presented study, a reference multiparameter equation of state (MPEoS) for carbon dioxide [25,26] has been chosen in order to compute the required thermodynamic properties. The increased number of parameters in MPEoSs allows for accurate computations of all relevant thermodynamic properties, with the highest possible accuracy, which is required for the design and analysis of advanced technical applications as well as scientific purposes [6]. While these complex EoS are very accurate, they are computationally expensive for the use in a general purpose Navier–Stokes solver. Therefore, all the required thermodynamic properties (and their derivatives) have been precomputed and stored in two tables (see Fig. 1(a)), one for the vapor–liquid and one for the single-phase region. The partitioning of the domain is necessary to limit the interpolation error close to the

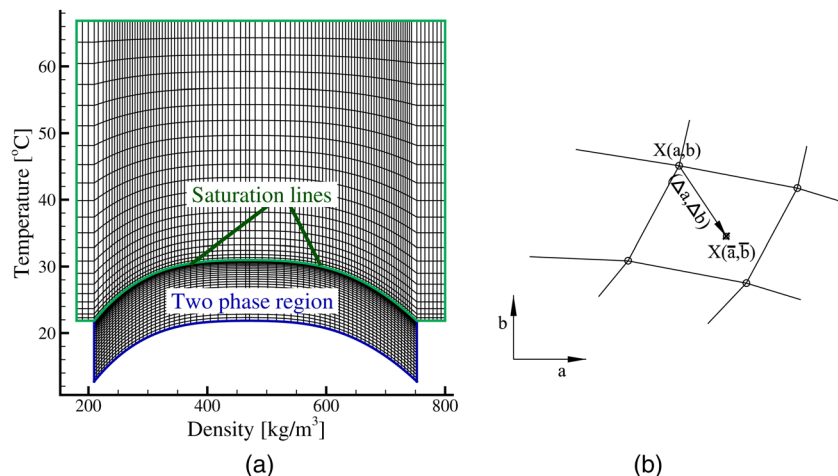


Fig. 1 The tabulated region in the temperature-density plane and schematic of the interpolation; (a) the tabulated region in the temperature-density plane, with the two tables which are separated by the saturation lines; (b) schematic of the interpolation applied in the look-up table

saturation line. In fact, when using a single table containing both regions, the interpolation error of some thermodynamic properties (e.g. speed of sound) may degrade the accuracy of Navier–Stokes solver.

In a preprocessing step the two tables are computed (for given boundary values of temperature and density) and stored in the memory. The saturation lines are also accurately computed and used each time the thermodynamic function is called to check which table must be used for the interpolation of the input state. During the simulation a look-up algorithm is used to compute the thermodynamic properties for a given set of two known properties that defines the thermodynamic state.

For any given pair of input values the cell containing the point is identified in the correct table. The interpolation is then performed using the gradient at the four nodes of the cell, with a successive distance-based averaging of the four interpolated values, that is

$$X(\bar{a}, \bar{b}) = \frac{\sum_{i=1}^4 \left(X(a_i, b_i) + \frac{\partial x}{\partial a} \Delta a_i + \frac{\partial x}{\partial b} \Delta b_i \right) / \sqrt{\Delta a_i^2 + \Delta b_i^2}}{\sum_{i=1}^4 1 / \sqrt{\Delta a_i^2 + \Delta b_i^2}} \quad (6)$$

where $X(\bar{a}, \bar{b})$ is a thermodynamic property interpolated for a given pair of independent properties \bar{a} and \bar{b} ; e.g., the pressure at a given density $\bar{\rho}$ and temperature \bar{T} reads $P(\bar{\rho}, \bar{T})$. Figure 1(b) shows a graphical representation of the interpolation given in Eq. (6). The weighted-least-squares gradient $(\partial x / \partial a, \partial x / \partial b)$ in Eq. (6) is approximated at all nodes of the table using eight neighbors for the interior nodes, and correspondingly less at the boundary of the tables. In order to speed up the interpolation, the least-squares coefficients are computed before the simulation starts.

The mean relative error for the interpolated pressure, speed of sound and enthalpy is shown in Fig. 2. A random set of 10,000 states was generated in the tabulated region as given in Fig. 1(a) and the interpolation was performed using as input the density ρ and the internal energy e . The error is defined as the L_1 -norm of the difference between the interpolated value and the direct evaluation of the equation of state model, divided by the local value and the number of random states used. The solid line represents the error using the gradient based interpolation, while the dashed line shows the error obtained using a standard bilinear interpolation scheme. For a low number of intervals (number of points in T and ρ) the more complex gradient based interpolation is slightly

superior compared to the bilinear interpolation scheme, while both schemes converge to the same error for a large number of intervals. Using 300 points in T and ρ leads to an error of 1×10^{-4} in pressure and 4×10^{-6} for the enthalpy. For the successive simulations of the centrifugal compressor the bilinear interpolation scheme was used with a table of 300 points in $T = [290, 323]$ K and 320 points in $\rho = [250, 600]$ kg/m³.

Geometry and Mesh Generation

The centrifugal impeller of the compressor stage operated at the Sandia scCO₂ [4] compression loop facility was investigated. The stage consisted of a centrifugal impeller with six main and six splitter blades, followed by 17 wedge shaped diffuser vanes. The radial gap between the impeller trailing edge and the leading edge of the diffuser vanes was approximately 0.3 mm. In the study presented herein we considered the impeller only. The vaned diffuser and the impeller tip clearance will be investigated in the near

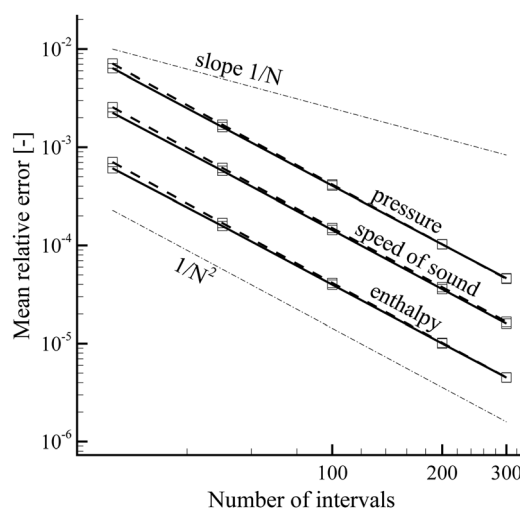


Fig. 2 Look-up table convergence and interpolation error using the density ρ and the internal energy e . The number of intervals is the same for the two independent variables. Dashed line represents a bilinear interpolation scheme, while the solid line shows the convergence rate for the interpolation scheme using the gradients at each surrounding node.

Table 1 Main impeller design dimensions [4]

Inlet shroud radius	9.37 (mm)
Inlet hub radius	2.53 (mm)
Exit blade height	1.71 (mm)
Exit blade radius	18.68 (mm)
Blade thickness	2 (mm)
Inlet blade angle at tip	50 (deg)
Exit blade back sweep angle	−50 (deg)

future. The main dimensions of the compressor are summarized in Table 1.

These dimensions together with part drawings were used to generate a 3D geometric model using the commercial blading software [27]. The obtained geometry was then transformed into a coordinate system such that the blade sections at each spanwise location was represented in two-dimensional planes. The axes of the transformed coordinate system are the normalized meridional length M (zero at the leading and one at the trailing edge, respectively), the azimuthal angle ϕ , and the normalized span height S .

A robust and fully automated hybrid mesh generator was developed to mesh the two-dimensional planes at various spanwise locations. First, a structured O-type mesh was wrapped around the transformed blade profiles with cells clustered towards the wall to resolve the boundary layers. Then, additional structured meshes were placed at the inlet and the outlet of the impeller and the remaining space between the structured meshes and the periodic boundaries was filled with triangles using a surface triangulation tool described in Ref. [28]. The surface triangulation was performed only at the hub ($S=0.0$) and morphed to the other spanwise locations ($S=0.25$, $S=0.5$, $S=0.75$, and $S=1.0$) to ensure the same triangulation topology (connectivity and number of triangles) in all planes. The morphing was done by adapting the boundary nodes of the unstructured mesh to match the nodes of the structured meshes at the next spanwise locations. Afterwards the unstructured mesh was relaxed using a Laplace-smoother. Finally, the two-dimensional meshes are transformed back into the Cartesian coordinate system, where they were used to obtain the cells in the spanwise direction through interpolation between these five layers.

The resulting three-dimensional mesh consists of hexahedral cells close to the blade walls and at the inlet and outlet of the impeller, and wedge cells elsewhere. The cells are clustered towards the walls

Table 2 Computational boundary conditions for nominal operation at $P_2 = 90$ bar and shaft speed = 50 krpm

Inlet velocity angle	0.0	(deg)
Static inlet pressure	76.9	(bar)
Static inlet temperature	305.974	(K)
Shaft speed	50,000.0	(rpm)
Static exit pressure	90.0	(bar)
Inlet turbulence intensity	5.0	(%)
Turbulent inlet Reynolds number	100.0	(-)

Table 3 Results for $P_2 = 90$ bar and shaft speed = 50 krpm

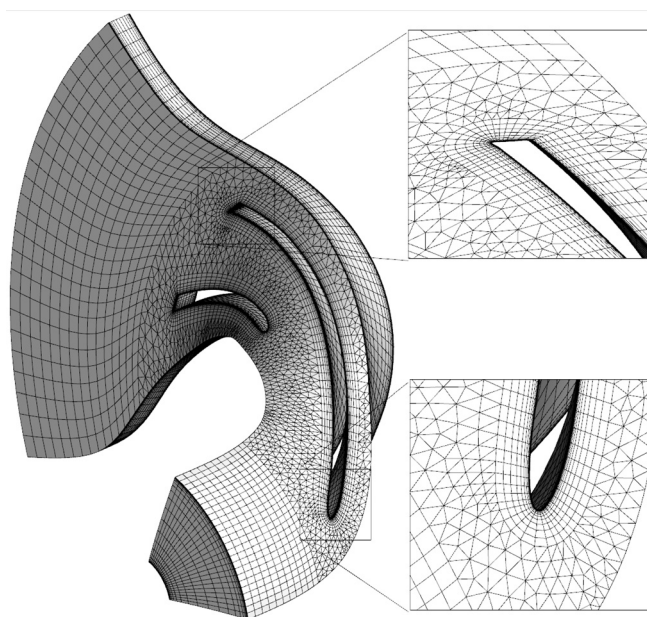
Mass flow	3.673	(kg/s)
Mass flow averaged exit enthalpy	324.015	(kJ/kg)
Efficiency	66.07	(%)

to ensure y^+ values close to unity. The total number of control volumes is approximately 340,000. The complete mesh for the impeller is shown in Fig. 3 together with detailed views of the mesh at the main blade leading and trailing edge at the shroud.

Results

First, results are shown for a single run using compressor inlet conditions as given in Ref. [29]. In the experimental campaign, compressor testing was done at several compressor shaft speeds from 25 to 60 krpm. The compressor is designed to operate with a shaft speed of 75 krpm and with a pressure ratio of 1.8. However, the most complete set of currently available data was obtained at 50 krpm shaft speed [29]. The inlet density is approximately 460 kg/m^3 and the inlet temperature during the experiment was held at a temperature between 304 and 306 K. The compressor operating conditions used for the simulation are summarized in Table 2. The exit pressure, used as a boundary condition for the simulations, was chosen such that the resulting mass flow rate was approximately $\dot{m} = 3.6 \text{ kg/s}$. Results for different back pressures are presented successively.

The $k-\omega$ SST turbulence model [11] was used for all simulations. The inlet turbulence intensity $Tu = \sqrt{u'^2}/U_{in}$, used to estimate the turbulent kinetic energy k , and the turbulent Reynolds number

**Fig. 3 Centrifugal compressor geometry and computational mesh**

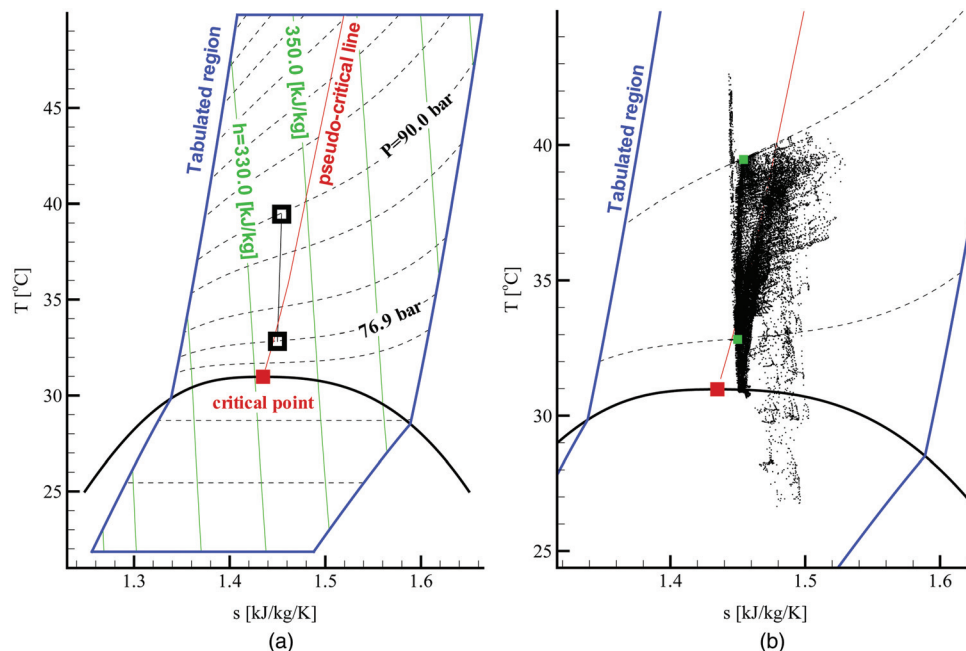


Fig. 4 Simulation results for $P_2 = 90$ bar and shaft speed = 50 krpm plotted in the $T - s$ diagram. (a) Averaged states of the compression process. The starting and the end state (black squares) of the compression are obtained by averaging the inlet and the outlet plane of the computational domain. (b) The point cloud represents all control volumes in the computational domain plotted in the T - s plane.

$Re_T = \rho k / (\mu C_\mu \omega)$, used to estimate the specific turbulent dissipation rate ω , are also given in Table 2. In future studies, an extended computational domain will be considered to take into account the slightly converging pipe section in front of the impeller. Also, fully developed turbulent velocity, turbulent kinetic energy k , and turbulent dissipation rate ω profiles could be used as inlet boundary conditions instead of the constant profiles for k and ω as currently used.

Additional details regarding the simulation are discussed hereafter. In turbulent flows the effective (total) thermal conductivity

is commonly modeled as the sum of the laminar and turbulent contributions, as

$$\lambda^{\text{eff}} = \lambda^l + \lambda^t, \text{ with: } \lambda^t = \frac{c_p \mu_t}{Pr_t} \text{ and } Pr_t = 0.9 \quad (7)$$

However, for turbulent flows close to the critical point the turbulent Prandtl number Pr_t is expected to vary significantly [30]. Since, based on the authors' knowledge, no models for the turbulent heat flux close to a fluid's critical point exist, we omitted λ^t in the energy equation of the Navier–Stokes equations. For heat transfer studies close to the critical point an accurate model for the turbulent heat flux has to be developed.

Table 3 summarizes the results for the mass flow rate, the mass flow averaged exit enthalpy, and the efficiency obtained for the nominal operating condition. A visual representation of the results is given in Fig. 4 by means of the entropy–temperature diagram. The black squares indicate the averaged states at the inlet and outlet conditions, connected with a line to represent the idealized compression of the supercritical CO_2 through the impeller. The compressor inlet conditions is located close to the liquid–vapor critical point and, moreover, very close to the pseudocritical line, Fig. 4(a). The pseudocritical line represents temperature and pressure conditions where peaks of the heat capacity c_p are observed due to vaporizationlike processes. The strong variations of the thermophysical properties in the vicinity of this line make the simulation a challenging task. Therefore, the convective fluxes in the Navier–Stokes equations are currently approximated using a first-order approach to increase the stability of the solver.

In Fig. 4(b) all control volumes present in the computational domain are plotted in the $T - s$ plane. Although, the compressor inlet condition is above the CO_2 saturation line, some fluid states also appear in the two-phase region. This is due to low pressures at the suction side close to the leading edge at the tip of the main blade, and in the wake-flow of the blade trailing edges, as also shown in Fig. 5.

In order to correctly take into account fluid condensation and its influence on the flow field, it is necessary to solve a system of

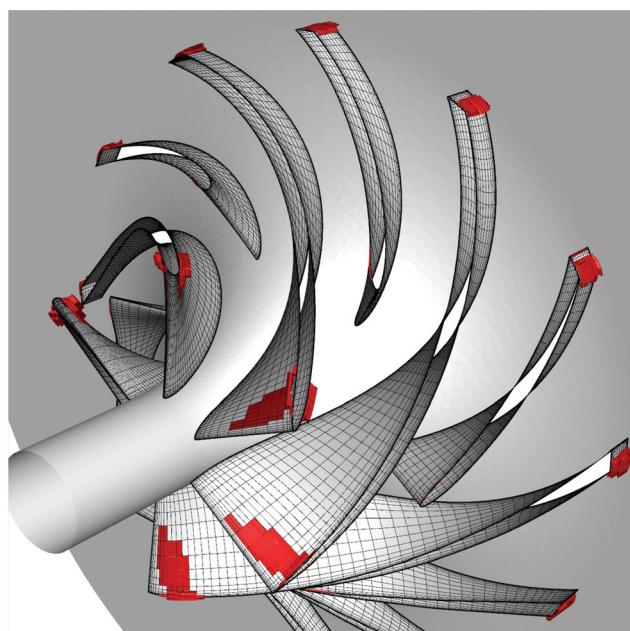


Fig. 5 The red surfaces show the two phase regions at the blade tip and the blade trailing edges for $P_2 = 90$ bar and shaft speed = 50 krpm

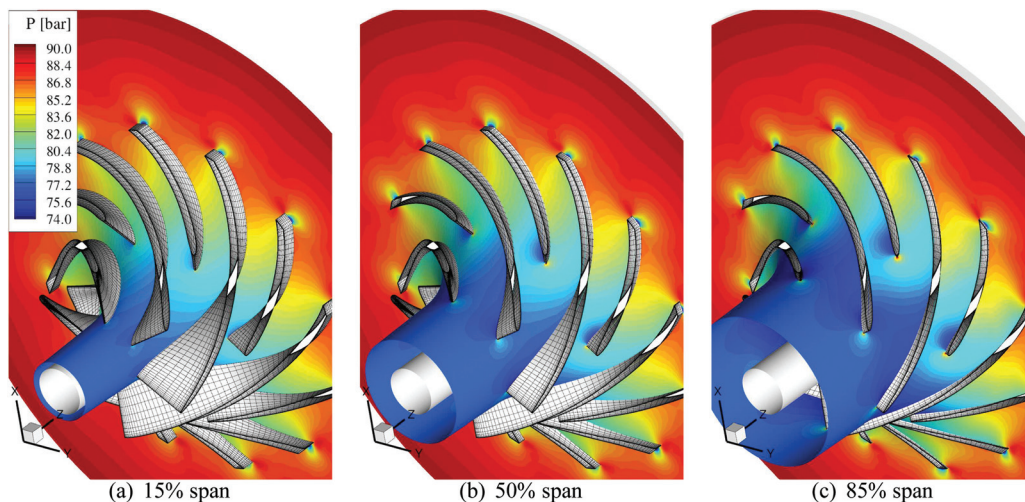


Fig. 6 Pressure contour plots in planes at different span locations for $P_2 = 90$ bar and shaft speed = 50 krpm

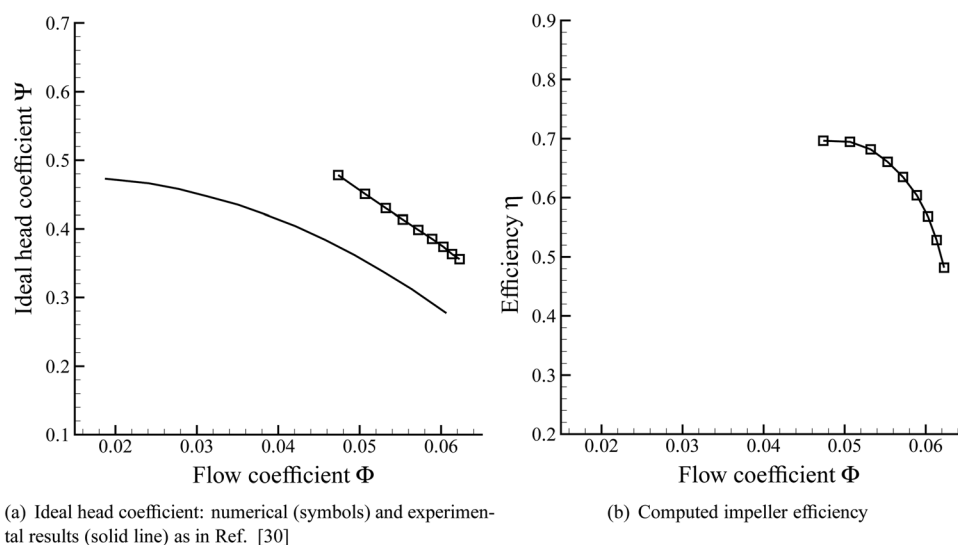


Fig. 7 Impeller performance for 50 krpm shaft speed

equations that describes both the gas and liquid phases. Essentially, two approaches exist: Euler/Euler and Euler/Lagrange. The former considers a homogeneous mixture of the gas and liquid phase, while the latter tracks the motion of the fluid elements for one of the two phases. An overview of these two strategies for viscous compressible flows can be found in Ref. [31]. Considering the Euler/Euler approach, source terms can be included in the conservation form of the Navier–Stokes system to account for mass transfer between gas and liquid, and a continuity equation for the gas phase only must be specified to close the problem [32,33]. In this study the correct dynamic of the condensation process has not been resolved for two main reasons. The first being the small region of the two phase flow, which should not affect significantly the results of the current simulations. The second is the lack of a condensation model suitable for fluid states slightly below the critical point and the absence of experimental data for which the simulation can be validated. It is expected that for higher rotational speeds, higher mass flows, and the presence of the tip clearance the regions in which liquefaction is predicted are considerably larger and an accurate description of fluid condensation becomes more important.

The points on the right-hand side of the averaged exit condition (green square in Fig. 4(b)) are related to regions within the boundary layers close to the diffuser outlet. The points on the left-hand side and above the exit condition are representing the stagnation pressures and temperatures at the leading edges of the main and splitter blades close to the shroud, where the peripheral velocity of the blades is the highest.

Figure 6 shows pressure contour plots in planes at different span-wise locations from the hub to the shroud, namely $S = 0.15$, $S = 0.5$, and $S = 0.85$. Regions of low pressure appear at the blade trailing edges and slightly downstream of the blade leading edges, where also condensation is observed. Generally, the contours show a smooth pressure increase through the impeller.

The impeller performance for 50 krpm shaft speed is shown in Fig. 7. The speed line was obtained by running simulations with exit pressures from 85 to 93 bar in increments of 1 bar. Simulations for higher pressure ratios showed the occurrence of stall in the vaneless diffuser section and the results are not shown here. Figure 7(a) displays the ideal head coefficient $\Psi = \Delta h / U_2^2$, plotted as a function of the flow coefficient $\Phi = Q / (\rho_1 U_2 D_2^2)$, and

compared to the experimental data; see Ref. [29]. As expected, due to the simplified geometry of the present simulations, the results show a higher head coefficient compared to the experiments. Simulations considering also the tip clearance, the diffuser vanes, and fully developed turbulent pipe flow profiles for the velocity and the turbulent quantities at the inlet will reduce the predicted head coefficient, and lead to a better agreement with measured values. These improvements are planned for a following study. The predicted impeller efficiency is shown in Fig. 7(b). The efficiency peaks at around 70%, which was also observed during the experiments, although at slightly lower values of the flow coefficient.

Conclusion

This paper presents a three-dimensional CFD study of the impeller of a centrifugal compressor operating with CO₂ in the thermodynamic region slightly above the vapor–liquid critical point.

In order to validate the real-gas solver, the geometry corresponding to an impeller tested in the Sandia scCO₂ compression loop facility [4] has been selected. A detailed evaluation of the CFD results was performed, and the results were compared to experimental data [29]. The ideal head coefficient computed from the results of the flow-field simulation was higher than the one computed from measurements, due to the simplified geometry adopted in this phase of the project. Future simulation studies will consider also the effect of the tip clearance, fully developed turbulent velocity profiles at the compressor inlet, and the increase of the pressure recovery due to diffuser vanes.

The simulations highlighted that future research also needs to focus on several fundamental aspects in order to improve the predictive capability of numerical simulations with fluids operated close to the critical point. For compressor operating conditions featuring higher shaft speeds, or for operating conditions entailing wet compressor inlet, the two-phase thermodynamic region and a complete and validated description of the condensation process are of major importance. Furthermore, current turbulence models do not take into account strong variations (density fluctuations) occurring close to the pseudocritical line. Improved models are needed, especially when accurate heat transfer predictions are relevant.

Acknowledgment

The authors would like to acknowledge the use of the high-performance computing facilities at Stanford University: MRI-R2, Acquisition of a Hybrid CPU/GPU and Visualization Cluster for Multidisciplinary Studies in Transport Physics with Uncertainty Quantification, National Science Foundation Award No. 0960306. The authors are also thankful to Dr. Steven A. Wright (former principal investigator of the Sandia project) for numerous interesting discussions on this topic.

Nomenclature

A = cell face area
 c_p = specific heat capacity at constant pressure
 e = internal energy
 \mathbf{F} = convective flux vector
 \mathbf{F}_v = viscous flux vector
 h = enthalpy
 k = turbulent kinetic energy
 \mathbf{n} = outward pointing unit vector normal to surface
 P = pressure
 Pr = Prandtl number
 Q = volumetric flow rate
 \mathbf{R} = residuum
 Re = Reynolds number
 r_f = vector connecting cell center and center of cell face

S = span location
 \mathbf{S} = source term vector
 T = temperature
 Tu = turbulence intensity
 t = time
 \mathbf{U} = vector of conserved variables
 U = peripheral velocity
 V = cell volume
 \mathbf{v} = Cartesian velocity vector
 \mathbf{x} = Cartesian position vector
 Φ = flow coefficient
 λ = thermal conductivity
 μ = absolute viscosity
 Ω = physical domain
 $\partial\Omega$ = boundary of the physical domain
 ω = specific turbulent dissipation, angular speed
 Π = stress tensor
 Ψ = ideal head coefficient
 ρ = density

Subscripts

1 = impeller inlet
 2 = impeller outlet
 eff = effective quantity
 f = cell face
 l = laminar quantity
 t = turbulent quantity
 P = cell center

References

- [1] Angelino, G., 1969, "Carbon Dioxide Condensation Cycles for Power Production," *ASME J. Eng. Power Trans.*, **10**, pp. 272–287.
- [2] Feher, E. G., 1968, "The Supercritical Thermodynamic Power Cycle," *Energy Convers.*, **8**, pp. 85–90.
- [3] Dostal, V., Driscoll, M. J., and Hejzlar, P., 2004, "A Supercritical Carbon Dioxide Cycle for Next Generation Nuclear Reactors," MIT-ANP-Series, Massachusetts Institute of Technology, Boston, MA, MIT-ANP-TR-100.
- [4] Wright, S. A., Radel, R. F., Vernon, M. E., Rochau, G. E., and Pickard, P. S., 2010, "Operation and Analysis of a Supercritical CO₂ Brayton Cycle," Sandia Report 2010-0171.
- [5] Colonna, P., Harinck, J., Rebay, S., and Guardone, A., 2008, "Real-Gas Effects in Organic Rankine Cycle Turbine Nozzles," *J. Propul. Power*, **24**(2), pp. 282–294.
- [6] Harinck, J., Colonna, P., Guardone, A., and Rebay, S., 2010, "Influence of Thermodynamic Models in 2D Flow Simulations of Turboexpanders," *ASME J. Turbomach.*, **132**(1), p. 011001.
- [7] Takagi, K., Muto, Y., Ishizuka, T., Kikura, H., and Aritomi, M., 2010, "Research on Flow Characteristics of Supercritical CO₂ Axial Compressor Blades by CFD Analysis," *J. Power Eng. Syst.*, **4**(1), pp. 138–149.
- [8] Pecnik, R., Terrapon, V. E., Ham, F., Iaccarino, G., and Pitsch, H., 2012, "Reynolds-Averaged Navier–Stokes Simulations of the Hyshot II Scramjet," *AIAA J.*, **50**(8), pp. 1717–1732.
- [9] Pečnik, R., Witteveen, J. A. S., and Iaccarino, G., 2011, "Uncertainty Quantification for Laminar-Turbulent Transition Prediction in RANS Turbomachinery Applications," 49th AIAA Aerospace Sciences Meeting, Orlando, FL, Jan. 4–7, AIAA Paper No. 2011-660.
- [10] Spalart, P. R., and Allmaras, S. R., 1992, "A One-Equation Turbulence Model for Aerodynamic Flows," AIAA Paper No. 92-0439.
- [11] Menter, F. R., 1994, "Two-Equation Eddy-Viscosity Turbulence Models for Engineering Applications," *AIAA J.*, **32**(8), pp. 1598–1605.
- [12] Satish, B., Buschelman, K., Eijkhout, V., Gropp, W. D., Kaushik, D., Knepley, M. G., McInnes, L. C., Smith, B. F., and Zhang, H., 2009, PETSc Web page, <http://www.mcs.anl.gov/petsc>
- [13] Berger, M., Aftosmis, M. J., and Murman, S. M., 2005, "Analysis of Slope Limiters on Irregular Grids," 43rd AIAA Aerospace Sciences Meeting, Reno, NV, Jan. 10–13, AIAA Paper No. 2005-0490.
- [14] Barth, T. J., and Jespersen, D. C., 1989, "The Design and Application of Upwind Schemes on Unstructured Meshes," AIAA Paper No. 89-0366.
- [15] Venkatakrishnan, V., 1995, "Convergence to Steady State Solutions of the Euler Equations on Unstructured Grids With Limiters," *J. Comput. Phys.*, **118**(1), pp. 120–130.
- [16] Roe, P. L., 1981, "Approximate Riemann Solvers, Parameter Vectors, and Difference Schemes," *J. Comput. Phys.*, **43**(2), pp. 357–372.
- [17] Candler, G. V., Barnhardt, M. D., Drayna, T. M., Nompelis, I., Peterson, D. M., and Subbareddy, P., 2007, "Unstructured Grid Approaches for Accurate Aero-heating Simulations," AIAA Paper No. 2007-3959.
- [18] Quirk, J. J., 1994, "A Contribution to the Great Riemann Solver Debate," *Int. J. Numer. Meth. Fluids*, **18**(6), pp. 555–574.

- [19] Van Leer, B., Lee, W. T., and Powell, K. G., 1989, "Sonic-Point Capturing," AIAA Paper No. 89-1945.
- [20] Nompelis, I., Drayna, T. W., and Candler, G. V., 2005, "A Parallel Unstructured Implicit Solver for Hypersonic Reacting Flow Simulation," AIAA Paper No. 2005-4867.
- [21] Liou, M.-S., 1996, "A Sequel to AUSM: AUSM+," *J. Comput. Phys.*, **129**(2), pp. 364–382.
- [22] Ham, F., and Iaccarino, G., 2004, "Energy Conservation in Collocated Discretization Schemes on Unstructured Meshes," Annual Research Briefs 2004, Center for Turbulence Research, NASA Ames/Stanford University, Stanford, CA.
- [23] Colonna, P., and Van der Stelt, T., 2005, "Fluidprop: A Program for the Estimation of Thermophysical Properties of Fluids," Energy Technology Section, Delft University of Technology, Delft, The Netherlands, available at: <http://www.fluidprop.com>
- [24] Lemmon, E. W., McLinden, M. O., and Huber, M. L., 2002, "NIST Standard Reference Database 23: Reference Fluid Thermodynamic and Transport Properties-REFPROP, Version 8.0," National Institute of Standards and Technology, Standard Reference Data Program, Gaithersburg, MD.
- [25] Span, R., and Wagner, W., 2003, "Equations of State for Technical Applications. I. Simultaneously Optimized Functional Forms for Nonpolar and Polar Fluids," *Int. J. Thermophys.*, **24**, pp. 1–39.
- [26] Span, R., and Wagner, W., 2003, "Equations of State for Technical Applications. II. Results for Nonpolar Fluids," *Int. J. Thermophys.*, **24**, pp. 41–109.
- [27] ANSYS, 2009, "ANSYS BladeGen, Release 13.0 Users Guide," ANSYS, Inc., Canonsburg, PA.
- [28] Shewchuk, J., 1996, "Triangle: Engineering a 2D Quality Mesh Generator and Delaunay Triangulator," *Applied Computational Geometry Towards Geometric Engineering* (Lecture Notes in Computer Science), Vol. 1148, M. Lin and D. Manocha, eds., Springer, Berlin/Heidelberg, pp. 203–222.
- [29] Fuller, R. L., and Eisemann, K., 2011, "Centrifugal Compressor Off-Design Performance for Super-Critical CO₂," Supercritical CO₂ Power Cycle Symposium, Boulder, CO, May.
- [30] Bae, J., Yoo, J., and Choi, H., 2005, "Direct Numerical Simulation of Turbulent Supercritical Flows With Heat Transfer," *Phys. Fluids*, **17**(10), pp. 1–24.
- [31] Sokolichin, A., Eigenberger, G., Lapin, A., and Lübbert, A., 1997, "Dynamic Numerical Simulation of Gas-Liquid Two-Phase Flows: Euler/Euler Versus Euler/Lagrange," *Chem. Eng. Sci.*, **52**(4), pp. 611–626.
- [32] Blesgen, T., 1999, "Generalization of the Navier–Stokes Equations to Two-Phase Flows," *J. Phys. D Appl. Phys.*, **32**(10), pp. 1119–1123.
- [33] Nikkhahi, B., Shams, M., and Ziabasharhagh, M., 2009, "A Numerical Investigation of Two-Phase Steam Flow Around a 2-D Turbine's Rotor Tip," *Int. Commun. Heat Mass Transf.*, **36**(6), pp. 632–639.